Human-machine collaboration: ordering mechanism of rank-2 spin liquid on breathing pyrochlore lattice

Nicolas Sadoune, Ke Liu, Han Yan, Ludovic D.C Jaubert, Nic Shannon, Lode Pollet

Human-machine collaboration: ordering mechanism of rank-2 spin liquid on breathing pyrochlore lattice

Nicolas Sadoune,[1,2] Ke Liu,[1,2,3,4] Han Yan,[5,6,7,8] Ludovic D.C. Jaubert,[9] Nic Shannon,[5] and Lode Pollet[1,2]

[1]*Arnold Sommerfeld Center for Theoretical Physics, LMU Munich, Theresienstr. 37, 80333 München, Germany*
[2]*Munich Center for Quantum Science and Technology (MCQST), 80799 München, Germany*
[3]*Hefei National Research Center for Physical Sciences at the Microscale and School of Physical Sciences, University of Science and Technology of China, Hefei 230026, China*
[4]*Shanghai Research Center for Quantum Science and CAS Center for Excellence in Quantum Information and Quantum Physics, University of Science and Technology of China, Shanghai 201315, China*
[5]*Theory of Quantum Matter Unit, Okinawa Institute of Science and Technology Graduate University, Onna-son, Okinawa 904-0412, Japan*
[6]*Institute for Solid State Physics, University of Tokyo, Kashiwa, 277-8581 Chiba, Japan*
[7]*Department of Physics and Astronomy, Rice University, Houston, TX 77005, USA*
[8]*Smalley-Curl Institute, Rice University, Houston, TX 77005, USA*
[9]*CNRS, Université de Bordeaux, LOMA, UMR 5798, 33400 Talence, France*

(Dated: February 19, 2024)

Machine learning algorithms thrive on large data sets of good quality. Here we show that they can also excel in a typical research setting with little data of limited quality, through an interplay of insights coming from machine, and human researchers. The question we address is the unsolved problem of ordering out of a spin–liquid phase described by an emergent rank–2 $U(1)$ gauge theory, as described by [H. Yan *et al.*, Phys. Rev. Lett. **124**, 127203 (2020)]. Published Monte Carlo simulations for this problem are consistent with a strong first–order phase transition, but were too noisy for the form of low-temperature order to be identified. Using a highly–interpretable machine learning approach based on a support vector machine with a tensorial kernel (TKSVM), we re-analyze this Monte Carlo data, gaining new information about the form of order that could in turn be interpreted by traditionally-trained physicists. We find that the low-temperature ordered phase is a form of hybrid nematic order with emergent Z_2 symmetry, which allows for a sub-extensive set of domain walls at zero energy. This complex form of order arises due to a subtle thermal order-by-disorder mechanism, that can be understood from the fluctuations of the tensor electric field of the parent rank-2 gauge theory. These results were obtained by a back-and-forth process which closely resembles a collaboration between human researchers and machines. We argue that this "collaborative" approach may provide a blueprint for solving other problems that have not yielded to human insights alone.

I. INTRODUCTION

Condensed matter physics has the fascinating property that phenomena which are difficult to realize in the natural world can emerge from complex models. Well-known examples are magnetic monopoles, which are natural excitations of spin-ice materials[1,2] and whose quantum fluctuations offer a tunable version of QED,[2–4] and Kitaev magnets, which support Majorana fermions.[5,6] Recently, there has been a flurry of activity in realizing even more exotic higher-rank gauge fields[7–9] as a source for fractons, which are excitations of reduced mobility emerging in novel types of topological order,[10–12] and which are also promising for quantum computing. Clearly, opening a window for strongly correlated physics, emergent gauge fields, and/or fractionalization, requires competing interactions hindering long-range order, which is the hallmark of frustration. A world of opportunity is therefore awaiting in frustrated magnets. However, precisely because of the wide range of possible outcomes, numerical simulations of frustrated magnets are notoriously difficult to perform, showing a strong tendency to fall out of equilibrium at low temperatures. And even where simulations converge, results can still be challenging to interpret. As a consequence, many interesting questions about the emergent phenomena found in frustrated models at low temperature remain out of reach.

Another area where great advances have been made in the past decade is in the application of machine learning techniques to complex data sets. Where it is interpretable, and can be trained without prior assumptions, machine learning can perform a role similar to a human researcher, constructing a classification scheme for different phases of matter "from scratch". A number of different calculations of this type have been carried out for frustrated models,[13–18] and have proved capable of reproducing complicated phase diagrams for systems with emergent gauge symmetry,[15,17] and even of identifying magnetic phases not previously anticipated by other means.[19] Nonetheless, how "AI" will impact on research into novel phases of matter, and the way in which it will change patterns of work, remains an open question.

This paper has two objectives: firstly, to solve a complex physics problem, in an active field of research related to emergent gauge fields; and secondly, to show how this solution becomes possible through an interaction between human and machine learning. The problem we consider is an archetypical "hard problem" in frustrated magnetism: using numerical simulation of a model which supports many (quasi–)degenerate states to identify a complex and previously unknown form of order at low temperatures. More specifically, we address the form of low–temperature magnetic order which descends from a spin liquid described by an emergent rank-2 gauge field, in a model motivated by breathing–pyrochlore magnets.

In earlier work by Yan *et al.* [Ref. 20], traditional methods based on the calculation of structure factors within Classical

Monte Carlo simulation, were used to establish both the existence of a rank–2 U(1) spin liquid at finite temperature, and to identify a transition into an ordered phase at low temperatures. However, this approach failed to pinpoint the form of low–temperature order, on account of difficulty of converging simulations at low temperatures. Here we revisit those simulations, and show what is gained by analyzing data using a variant of a support vector machine with tensorial kernel (TKSVM).[14–16] This highly–interpretable form of machine learning is employed without prior training or supervision. Through a step-by-step iteration of the insights derived from human and machine learning, we are able to successfully identify both the unknown ground state order, and the mechanism through which it occurs. We argue that this back–and–forth process resembles a collaboration between human researchers and "machine", an approach which may yield success in other difficult research problems.

The model in question is the Heisenberg antiferromagnet on the breathing pyrochlore lattice with Dzyaloshinskii-Moriya (DM) interactions on alternating tetrahedra is known to support a rank-2 gauge field theory.[20,21] Descending from this higher-rank gauge field, Monte Carlo simulations showed the onset of an undefined magnetic order at very low temperature, $T_c \sim 10^{-3}J$ where J is the antiferromagnetic exchange coupling [Fig. 2]. The model is essentially a "worst-case scenario" for Monte Carlo (MC) simulations, where a joint heatbath, parallel-tempering and overrelaxation algorithm could not satisfactorily thermalise the ordered phase [Fig. 3]. We believe this difficulty to thermalize is revealing of the naturally complex magnetic texture of a higher-rank gauge field, making our approach a test case for such questions. This is where AI helped us extract the relevant information out of noisy and incomplete numerical data and, together with analytical support, refine the MC simulations.

As a summary, we have found the nature of the long-range ordered phase, as illustrated in Fig. 1a. The machine could identify two distinct order parameters that brought to light a two-step ordering mechanism. First a traditional energetic selection into a continuously degenerate ground state manifold, followed by an entropic selection via thermal order by disorder.[22,23] Initializing the Monte Carlo simulations with the learned structure has led to well converged data [Fig. 8]. Another iteration of human-machine collaboration then unveiled a zero-energy sub-extensive dynamics, which is neither a global nor local symmetry of the system, but an emergent Z_2 subsystem symmetry [Fig. 9]. The emergence of a sub-extensive symmetry is markedly unusual for a realistic two-body Hamiltonian, since it typically requires an artificially complex set of interactions, as seen e.g. in fractonic matter.[10–12] As a consequence, this sub-extensive symmetry leads to a hybridization of linear (dipolar) and quadratic (quadrupolar) magnetic orders. The dipolar order breaks spin-rotation, spin-permutation and translational symmetries, while the quadrupolar order additionally breaks lattice-rotation symmetry giving rise to an emergent nematicity. Finally, we could rationalize the order parameters found by the machine as descending from fluctuations of the tensor electric field $\mathbf{E}$ of the rank-2 gauge theory.

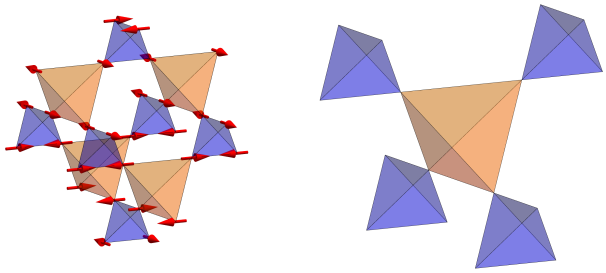

(a) (b)

FIG. 1. **(a) Ground-state spin configuration.** The breathing pyrochlore lattice is made of two inequivalent types of corner-sharing tetrahedra, labeled by A in blue and B in red. Our model consists of nearest-neighbor interactions, with antiferromagnetic exchange everywhere, and Dzyaloshinskii-Moriya (DM) interactions on A-tetrahedra only [Eq. 1]. The ground state is coplanar and nematic in the sense that it breaks lattice-rotation symmetry. The ordering mechanism comes from a thermal order-by-disorder selection within the emergent rank-2 U(1) gauge field. See App. A for relevant definitions. **(b) The FCC cubic unit cell** comprises 16 sites forming four A- and one B-tetrahedron. Considering the centre of the four $A-$tetrahedra, it forms the minimal unit cell of the face-centred-cubic (FCC) lattice. This cluster will be used for analysing rank-2 results.

II. MODEL

The model is a classical Heisenberg antiferromagnet on the breathing pyrochlore lattice, decorated by DM interactions on one of the two types of tetrahedra [Fig. 1a]. The Hamiltonian reads as follows:

$$H = J\sum_{\langle ij\rangle} \boldsymbol{S}_i \cdot \boldsymbol{S}_j + D\sum_{\langle ij\rangle\in A} \boldsymbol{d}_{ij}\cdot(\boldsymbol{S}_i\times\boldsymbol{S}_j). \qquad (1)$$

The position of sites as well as the DM vectors $\boldsymbol{d}_{ij}$ are specified in App. A. The model came to prominence because of the possibility of realizing an exotic rank-2 $U(1)$ spin liquid for negative $D<0$.[20] Furthermore, materials such as $Ba_3Yb_2Zn_5O_{11}$ have parameters in this regime for the A-tetrahedra, although the antiferromagnetic interactions on the B-tetrahedra might be too small.[24–26] For $J_B = J_A = J = 1$ and $D = 0$ the model reduces to the standard Heisenberg antiferromagnet on the pyrochlore lattice, displaying the well-understood rank-1 classical spin liquid behavior for $T\to 0$, and this behavior crosses over at higher temperature to a standard paramagnet.

For positive $D > 0$, the ground state is a simple all-in all-out ordered phase at low temperature.[20] However, at negative $D <$ 0 below the rank-2 $U(1)$ spin liquid, the system was found to order in some fashion that was ill understood because of thermalisation issues. All that was known was the presence of Bragg peaks in the structure factor at finite $\mathbf{q} = W$ wavevector, possibly co-existing with other phases. The properties of this phase are the subject of this paper, and we shall fix $J = 1$ and $D = -0.0141$.

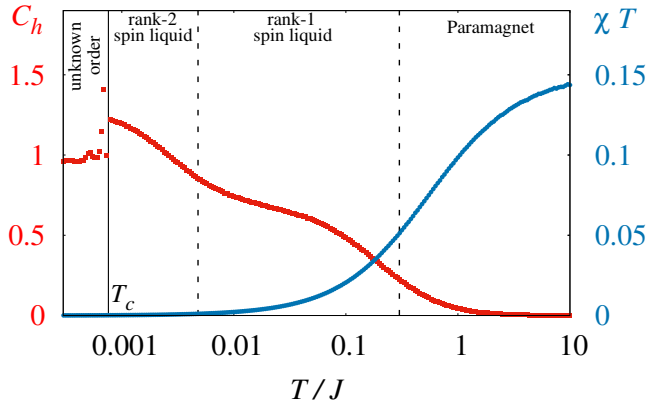

FIG. 2. **The phase diagram** of our model presents three distinct regimes before ordering upon cooling:[20] a paramagnet, a rank-1 spin liquid (the Heisenberg antiferromagnet) and a rank-2 spin liquid, as illustrated from the evolution of the specific heat C_h (red) and reduced susceptibility χT (blue). The ordered phase is separated from paramagnetic fluctuations by three orders of magnitude in temperature T. The vertical dashed and solid lines are respectively crossovers and a phase transition. Our goal is to understand the nature of the "unknown order" below the transition at T_c. The system size is $N = 8192$, the DM term is set to $D = -0.0141J$ and the $x-$axis is in logarithmic scale.

III. SIMULATIONS BEFORE AI INPUT

We performed Monte Carlo simulations following the procedure of Ref. 20 for system size up to 27 648 spins ($N = 16L^3$) of length $|S| = 1/2$. Starting from a random spin configuration, the system is annealed from high temperature to a temperature T during 10^6 Monte Carlo steps, then thermalised at T for another 10^6 Monte Carlo steps, and finally data are collected for statistical averaging during 10^7 MC steps. Each MC step is made of N single-spin-flip updates via the rejectionless heatbath algorithm and five overrelaxation updates sweeping through the entire lattice. Overrelaxation is a microcanonical update with spin rotation around the local molecular field for each spin; we include both π rotations (the largest one) and random ones. Every 100 MC steps, there is parallel tempering between neighbouring temperatures (126 temperatures in parallel between $T = 0$ and $0.0025J$). Based on our experience with classical Monte Carlo simulations, in addition to the generic and rather powerful overrelaxation and parallel-tempering algorithms, these simulation parameters are an order of magnitude longer in time and bigger in system size than what is usually necessary to completely characterise a typical phase transition in a frustrated magnet. Nonetheless, we see in Fig. 3 that while it is possible to spot the presence of long-range order, we cannot properly thermalise the magnetic order at very low temperatures. As a consequence it is unclear if the order with Bragg peaks at $\mathbf{q} = W$ is really (part of) the ground state and if it co-exists, or not, with other phases.

The reasons for this issue are multiple. On a fundamental level, our problem is the ordering mechanism descending from a higher-rank gauge field. As was shown in Ref. 20, the rank-2 gauge field itself descends from a rank-1 gauge field with a broader phase space manifold, namely the Coulomb spin liquid of the Heisenberg antiferromagnet on pyrochlore. It is the DM term on $A-$tetrahedra of Hamiltonian (1) that selects the rank-2 gauge field. This means that the ordered phase we are investigating is separated from paramagnetic fluctuations by *two* successive crossovers into more and more constrained configurational manifolds [Fig. 2]. Monte Carlo simulations are thus particularly constrained in phase space around T_c and can easily be trapped in local free-energy minima.

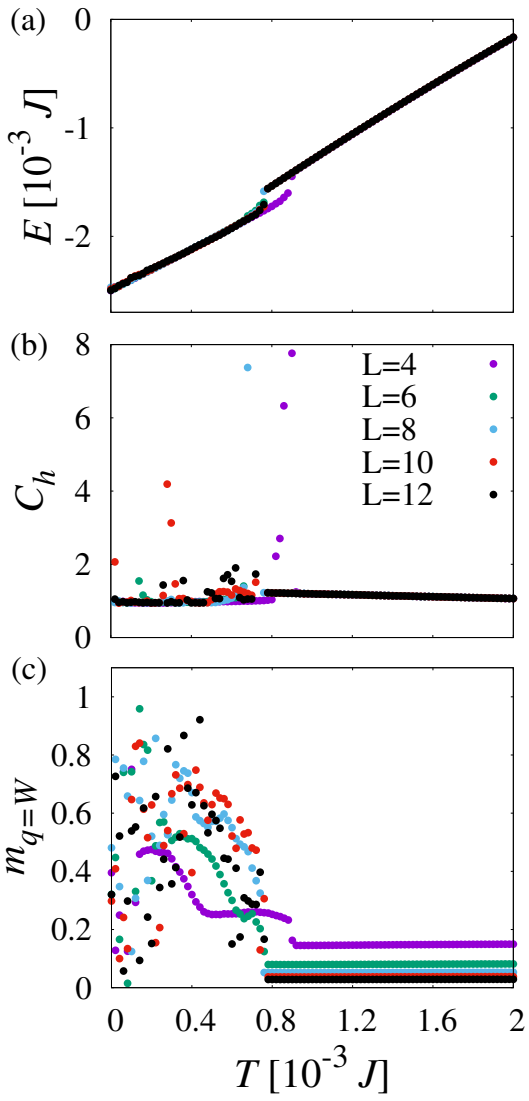

FIG. 3. **Monte Carlo simulations before AI input** show a phase transition at $T_c \approx 8.\,10^{-4}J$ in the (a) energy, (b) specific heat and (c) order parameter for wavevector $\mathbf{q} = W$ order (corners of the Brillouin zone) for system size $L \in \{4, 6, 8, 10, 12\}$. Simulations have been slowly annealed from high temperature during thermalisation. There are, however, noticeable finite-size effects and thermalisation issues below $T \sim 10^{-3}J$. Details of simulations are given in Sec. III. The energy in panel (a) has been shifted by $+J\,S^2 = +1/4$ for convenience.

This is where parallel tempering would usually help, by shuffling spin configurations across temperatures. But here the issue is not only that the transition temperature is far from paramagnetic fluctuations. The visible jumps in energy and order parameter in Fig. 3(a,c) suggest a first-order transition. This strongly hinders the efficiency of parallel tempering, because the discontinuity in energy essentially prevents spin configurations from crossing the transition temperature. Hence one cannot rely on parallel tempering to help thermalise the ordered phase. In addition, the energy jump in Fig. 3(a) is of the order of $10^{-4}J$. Such a tiny energy selection is consistent with the double crossover mentioned above but, keeping in mind that we are at proximity of a highly degenerate spin liquid, it also suggests a competition between multiple phases that are quasi-degenerate in free energy. Finally, the $\mathbf{q} = W$ Bragg peaks implies a large magnetic unit cell made of 32 sites, which is another complication in itself for the local heatbath algorithm.

Our point is that, even if not necessarily systematic, we expect thermalization issues to be relatively natural consequences of higher-rank gauge fields. Being governed by tensorial constraints and a multiplicity of conserved quantities, these exotic phases are inherently complex, and it comes as to no-surprise for their ordering mechanisms to be unconventional. With these caveats in mind, our goal is to show how AI is able to help us, taking advantage of what it does best: extracting useful information out of noisy and incomplete data.

IV. THE MACHINE LEARNING ALGORITHM

Our machine learning algorithm, the tensorial kernel support vector machine (TKSVM), has been developed in Refs. 14,16,15. The inner working of the TKSVM algorithm are not necessary to understand the present work, as there are no algorithmic developments here, and we refer to App. B for a concise introduction to the method. It is, however, important to know its input requirements and output. TKSVM takes as input Monte Carlo snapshots of the spin configurations (typically 500-1000 of them) between two different data sets. Since the Hamiltonian parameters are fixed, we will compare different temperatures, in particular above and below T_c. It also requires as input the definition of a (typically small) cluster of sites, specified by the user. TKSVM builds on these clusters on a tensorial basis up to a predefined rank. Rank one can be thought of as dipolar magnetic order, rank two as quadrupolar order etc. The stochastic quantities defined on this cluster are obtained by averaging spin configurations over the full lattice. This significantly reduces the data's dimension to a dependence on the size of the cluster. The output of TKSVM is the decision function used to separate data into sets with different characters. This comprises structure factors (in the term of a coefficient matrix) and a bias term. The bias, usually used to extract phase diagrams by TKSVM, plays no role in this work. The structure factors encode the order parameters squared, and can be interpreted by the user. In other words, in the (simplified) setting when the machine strips all the information differentiating two data sets down to a single scalar, the decision function encodes the local order parameter of Landau theory reflecting symmetry breaking between the two data sets. An additional strength of TKSVM is that even in the absence of order, it is able to measure local constraints hinting at a potential classical spin liquid candidate. The extent of the locality, for both the order parameter and the spin-liquid constraint, is limited by the cluster size. As an illustrative example we refer to Ref. 15 where TKSVM successfully reproduced the phase diagram of the classical XXZ model on the pyrochlore lattice computed by Taillefumier et al.:[27] it found, and interpreted, the ordered in-plane ferromagnetic and nematic phases, but also identified and interpreted the crossovers between the high-temperature paramagnet and spin-ice, as well as the one with the Heisenberg spin liquid. Given this success and the tensorial nature of the higher-rank gauge fields, TKSVM is our method of choice to tackle this conundrum.

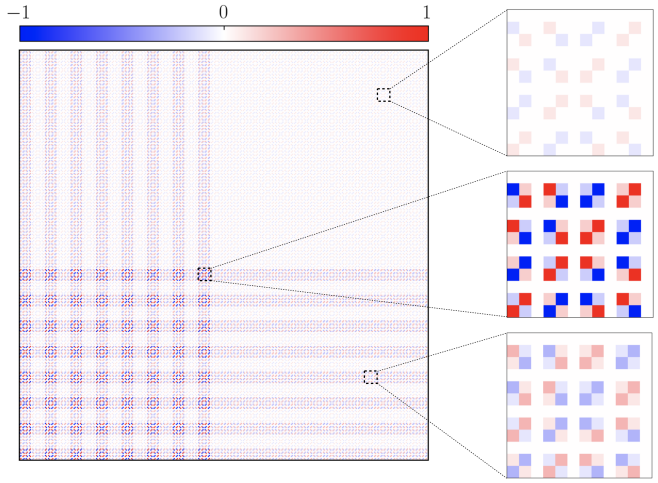

FIG. 4. **Rank-1 coefficient matrix.** On the x- and y-axis are all possible spin components $\{S_1^x, S_1^y, S_1^z, S_2^x, \ldots, S_{128}^z\}$, ommitted because of the large size of the matrix. Every entry of the 384×384 matrix represents the weight of a contraction $S_i^a S_{i'}^{a'}$ assigned by TKSVM during the learning process. Left: Full rank-1 pattern based on a $128-$site cluster (8 cubic unit cells). Right: Zoom into three different spin-contraction blocks with specific spin indices i, i', revealing similar structure but different overall magnitude.

A. Rank-1 results

Without prior knowledge of the phase, it is natural to start with the rank-1 kernel to probe potential magnetic orders. Rank-1 means that we consider quantities which are linear combinations of the spin components of the cluster, or in other words dipolar forms of magnetic order. As the complexity of the feature vector grows linearly at rank-1,[16] we can use very large clusters consisting of multiple lattice unit cells. Provided a phase is purely magnetic and has a perfect translational symmetry, the rank-1 patterns learned with different cluster sizes should converge to a stable, regular, structure. The magnetic order parameter can then be inferred and justified a posteriori

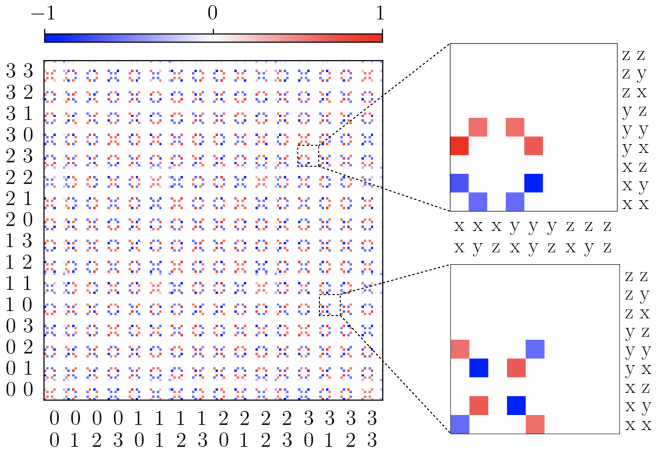

FIG. 5. **Rank−2 coefficient matrix** of d_A^{xy} for the $A-$ tetrahedra. In this example, spins are constrained in the spin xy plane. The dimension of the matrix is 144×144.

by measuring it in new Monte Carlo simulations.

However, in the unknown phase below T_c, we do not observe evidence of a stable rank−1 pattern even when using very large clusters up to 128 sites in Fig. 4. Instead, the learned patterns display sample-dependent irregular weights that are inconsistent with long-range dipolar order. This suggests that magnetic orders do not reflect the correlations in the system fully, and we shall further inspect the data at rank−2.

B. Rank−2 results

Rank−2 means that we consider quantities which are quadratic combinations of the spin components of the cluster, or in other words quadrupolar forms of magnetic order. The choice of the cluster at rank−2 is also guided by the lattice structure. Natural choices include a single A-tetrahedron, single B-tetrahedron, and FCC cubic unit cells of the breathing pyrochlore lattice consisting of 16 spins [see Fig. 1b]. We found that considering the A-tetrahedron and B-tetrahedron separately reveals all the information of the phase. After obtaining results for these clusters separately, they need to be combined to understand the structure of the ground states. Alternatively, using a FCC unit cell as a cluster directly reveals the ground state structure, at the price of a more involved interpretation and some redundancy from the four A-tetrahedra contained in the cluster. For simplicity, we will present the information extracted from A- and B-tetrahedra successively.

For each of the four A-tetrahedra, the (sub-)decision function is

$$d_A^s \sim (c_1^s)^2 + (c_2^s)^2, \tag{2}$$

where $s \in \{xy, yz, zx\}$ labels a global spin plane which spontaneously breaks the spin permutation symmetry of the Hamiltonian [Eq. (1)]. The precise order is thus defined by two effective order parameters c_1 and c_2 that are quadratic functions of spin components,

$$\begin{aligned} c_1^{yz} &= \frac{1}{16}\left((S_0^y - S_1^y + S_2^z - S_3^z)^2 + (S_0^z - S_1^z - S_2^y + S_3^y)^2\right) \\ c_1^{xz} &= \frac{1}{16}\left((S_0^x + S_1^z - S_2^x - S_3^z)^2 + (S_0^z - S_1^x - S_2^z + S_3^x)^2\right) \\ c_1^{xy} &= \frac{1}{16}\left((S_0^x + S_1^y - S_2^y - S_3^x)^2 + (S_0^y - S_1^x + S_2^x - S_3^y)^2\right) \end{aligned} \tag{3}$$

$$\begin{aligned} c_2^{yz} &= \frac{2}{16}(S_0^y - S_1^y + S_2^z - S_3^z)(S_0^z - S_1^z - S_2^y + S_3^y) \\ c_2^{xz} &= \frac{2}{16}(S_0^x + S_1^z - S_2^x - S_3^z)(S_0^z - S_1^x - S_2^z + S_3^x) \\ c_2^{xy} &= \frac{2}{16}(S_0^x + S_1^y - S_2^y - S_3^x)(S_0^y - S_1^x + S_2^x - S_3^y). \end{aligned} \tag{4}$$

As TKSVM is conceived to learn the optimal order parameters, we can reversely infer maximally ordered spin configurations by maximizing d_A^s. These fully ordered states are potential ground states. Note that in order to facilitate the interpretability of TKSVM we shall not average over Monte Carlo samples in which different spin planes are spontaneously selected; in fact, it suffices to analyze all samples separately. With no loss of generality, we consider a state where the ordering develops in the spin xy plane, whose corresponding TKSVM pattern (coefficient matrix) is illustrated in Fig. 5. The extraction of an analytical expression for the decision function from its graphical representation is discussed in App. C.

The form of the Eq. (2) suggests c_1^s and c_2^s can be viewed as independent order parameters. Therefore, we can maximize them separately and then check the consistency of their solutions. First, maximizing $(c_1^{xy})^2$ (i.e. solving $(c_1^{xy})^2 = 1$) leads to a manifold of spin configurations parametrized by an angle $\theta \in [0, 2\pi]$,

$$\begin{aligned} \boldsymbol{S}_0 &= \begin{pmatrix} \cos\theta \\ \sin\theta \\ 0 \end{pmatrix} \quad \boldsymbol{S}_1 = \begin{pmatrix} \cos\theta + \frac{\pi}{2} \\ \sin\theta + \frac{\pi}{2} \\ 0 \end{pmatrix} \\ \boldsymbol{S}_2 &= \begin{pmatrix} \cos\theta - \frac{\pi}{2} \\ \sin\theta - \frac{\pi}{2} \\ 0 \end{pmatrix} \quad \boldsymbol{S}_3 = \begin{pmatrix} \cos\theta + \pi \\ \sin\theta + \pi \\ 0 \end{pmatrix}, \end{aligned} \tag{5}$$

as illustrated in Fig. 6a. Maximizing $(c_2^{xy})^2$ falls into the same structure of Eq. (5). Its evolution as a function of θ is plotted in Fig. 6b and shows that $(c_2^{xy})^2$ is maximised for four discrete values only:

$$\theta \in \left\{\frac{\pi}{4}, \frac{3\pi}{4}, \frac{5\pi}{4}, \frac{7\pi}{4}\right\}. \tag{6}$$

The U(1) manifold of Eq. (5) belongs to the ground state of the traditional pyrochlore antiferromagnet with negative DM interactions on *all* tetrahedra,[28–30] i.e. without breathing anisotropy. Indeed, applying the spin configuration of Eq. (5) to Hamiltonian (1), we recover its ground-state energy per bond[28]

$$E_A^{\text{bond}} = \frac{1}{6}(-2J + 2\sqrt{2}D). \tag{7}$$

Spatial layer	Maximal weight	$(\boldsymbol{S}_0 \cdot \boldsymbol{S}_1)$	$(\boldsymbol{S}_0 \cdot \boldsymbol{S}_2)$	$(\boldsymbol{S}_0 \cdot \boldsymbol{S}_3)$	$(\boldsymbol{S}_1 \cdot \boldsymbol{S}_2)$	$(\boldsymbol{S}_1 \cdot \boldsymbol{S}_3)$	$(\boldsymbol{S}_2 \cdot \boldsymbol{S}_3)$	missing config.
yz	$w_1 = 1$	-1	± 1	∓ 1	∓ 1	± 1	-1	$P(\mathbf{\Lambda}_E^{\star 1}) = 0$
xz	$w_2 = 1$	± 1	-1	∓ 1	∓ 1	-1	± 1	$P(\mathbf{\Lambda}_E^{\star 2}) = 0$
xy	$w_3 = 1$	± 1	∓ 1	-1	-1	∓ 1	± 1	$P(\mathbf{\Lambda}_E^{\star 3}) = 0$

TABLE I. **Collinear ground states on B-tetrahedra.** In each case there are two possible solutions, reflecting the Z_2 symmetry. The leftmost column describes which spatial layer possesses the Z_2 symmetry, while the rightmost column indicates which of the three possible configurations of the B-tetrahedra, defined in Eq.(23), is not allowed.

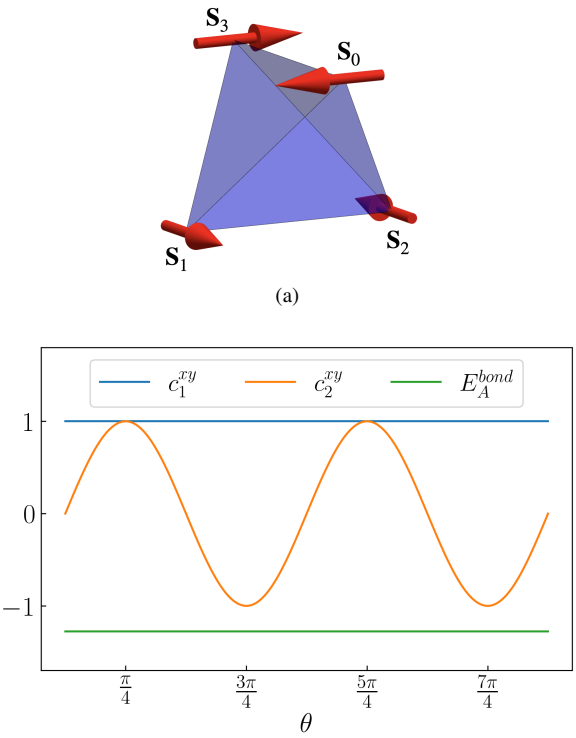

FIG. 6. **Order-by-disorder in $A-$tetrahedra.** (a) Example of a state maximising both c_1^{xy} and c_2^{xy} with $\theta = 7\pi/4$ in Eq.(5). The bonds that lie inside the spin-plane ($0-3$ and $1-2$) have anti-parallel spins. (b) The spin-plane-specific quantities c_1^{xy} and c_2^{xy} as well as the energy per bond [Eq. (7) with $J = 1$ and $D = -2$] as functions of the parametrisation angle θ. Note that in the decision function Eq. (2) the term c_2^{xy} appears squared, meaning that configurations with $c_2^{xy} = -1$ are also maxima of the decision function.

Since Eq. (7) is independent of θ, any selection of specific θ values is necessarily due to thermal order by disorder (ObD), i.e. the selection is entropic rather than energetic. In the standard model without breathing anisotropy, the ObD mechanism selects the $\mathbf{q} = 0$ ψ_3 long-range order,[28–30] which corresponds to θ equals to either $\frac{3\pi}{4}$ or $\frac{7\pi}{4}$ for all tetrahedra, and is illustrated in Fig. 6a. However, in our model where DM terms disappear on $B-$tetrahedra, the ground-state manifold is enlarged and the machine finds two additional solutions on the $A-$tetrahedra, $\theta \in \left\{\frac{\pi}{4}, \frac{5\pi}{4}\right\}$.

The ordering mechanism is thus a two-step process; first, the selection of the $U(1)$ manifold [Eq. (5)], and second, the coalescence on special points of the manifold via thermal order-by-disorder [Eq. (6)]. It is remarkable that the machine is able to extract both sets of solutions, by which we can infer the order-by-disorder phenomenon, out of noisy numerical data.

Now let us focus on the other type of tetrahedra, with only antiferromagnetic couplings (no DM terms). The (sub-)decision function on the B-tetrahedra is identified as

$$d_B \sim \big[\, w_1 \left(\mathbf{S}_0 \cdot \mathbf{S}_1 + \mathbf{S}_2 \cdot \mathbf{S}_3\right) + w_2 \left(\mathbf{S}_0 \cdot \mathbf{S}_2 + \mathbf{S}_1 \cdot \mathbf{S}_3\right) + w_3 \left(\mathbf{S}_0 \cdot \mathbf{S}_3 + \mathbf{S}_1 \cdot \mathbf{S}_2\right)\big]^2. \quad (8)$$

The values of the weights w_1, w_2, w_3 can be read off from the TKSVM patterns, satisfying

$$w_1 + w_2 + w_3 = 1, \quad \max w_i = 1, \quad (9)$$

where the maximal w_i is related to the ordering spin plane in d_A^s. Under this constraint, d_B can be intuitively maximized if the four spins in a B-tetrahedron are *collinear*. The solutions are listed in Table I, and Fig. 7a shows an example of the coefficient matrix when the ordering is in the spin xy plane with $w_3 = 1$.

Alternatively, the collinearity on the B-tetrahedra can also be derived from the constraints on the $A-$tetrahedra derived in the previous section. Without losing generality, we again take d_A^{xy} as an example. The four solutions of $\left(c_2^{xy}\right)^2 = 1$ can be divided into two classes

$$c_2^{xy} = 1: \quad \boldsymbol{S}_0 = \frac{1}{\sqrt{2}}\begin{pmatrix}1\\1\\0\end{pmatrix} \quad \boldsymbol{S}_1 = \frac{1}{\sqrt{2}}\begin{pmatrix}-1\\1\\0\end{pmatrix} \quad \boldsymbol{S}_2 = \frac{1}{\sqrt{2}}\begin{pmatrix}1\\-1\\0\end{pmatrix} \quad \boldsymbol{S}_3 = \frac{1}{\sqrt{2}}\begin{pmatrix}-1\\-1\\0\end{pmatrix}, \quad (10)$$

$$c_2^{xy} = -1: \quad \boldsymbol{S}_0 = \frac{1}{\sqrt{2}}\begin{pmatrix}1\\-1\\0\end{pmatrix} \quad \boldsymbol{S}_1 = \frac{1}{\sqrt{2}}\begin{pmatrix}1\\1\\0\end{pmatrix} \quad \boldsymbol{S}_2 = \frac{1}{\sqrt{2}}\begin{pmatrix}-1\\-1\\0\end{pmatrix} \quad \boldsymbol{S}_3 = \frac{1}{\sqrt{2}}\begin{pmatrix}-1\\1\\0\end{pmatrix}, \quad (11)$$

up to a global sign flip which preserves the value of c_2^{xy}. Eqs. (10) and (11) correspond to $\theta \in \left\{\frac{\pi}{4}, \frac{5\pi}{4}\right\}$ and $\left\{\frac{3\pi}{4}, \frac{7\pi}{4}\right\}$

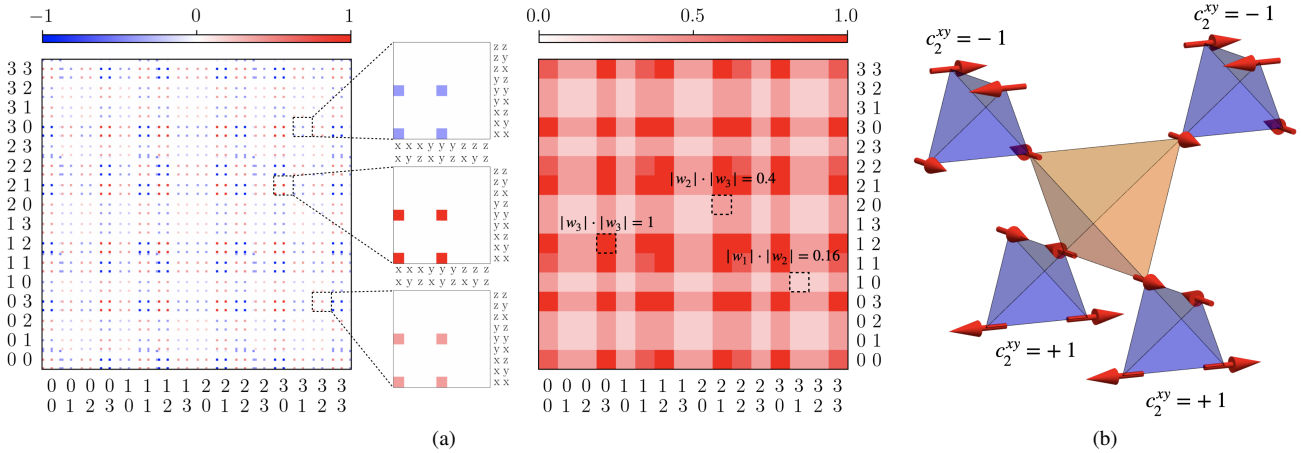

FIG. 7. **(a) Rank−2 coefficient matrix** of d_B for the $B-$ tetrahedra. Left: All blocks have the same structure but different weights. In this example, the z-component is missing because of the global spin-plane selection. Right: Absolute block-weight products of the left pattern. **(b) Ground-state configuration** with ordering in the xy plane. The value of c_2^{xy} is uniform within a A-tetrahedron layer, but alternates over different layers (cf. the upper two blue tetrahedra vs the lower two). In this example, the spin ordering plane coincides with the spatial plane.

respectively. Measurements of this machine-learned quantity show that $c_2^{xy} = \pm 1$ *alternates* through the z direction, as shown in Fig. 7b. As a B-tetrahedron shares spins with four A-tetrahedra, it has to take two collinear spins from Eq. (10) and then two spins with the same collinearity from Eq. (11). Otherwise, it cannot satisfy the staggered distribution $c_2^{xy} = \pm 1$. This long-range order breaks spin-rotation, spin-permutation and translational symmetry.

V. SIMULATIONS AFTER AI INPUT

Equipped with the patterns learned by the machine learning algorithm and the corresponding algebraic expressions, we go back to the Monte Carlo simulations. The simulations are now not slowly annealed from high temperature, but rather quenched into the configuration of Fig. 1a at temperature T, followed by 10^6 MC steps of thermalisation, and 10^7 MC steps for measurements. Paving the lattice with the ground state found by the machine requires alternating along the z direction, the $xy-$layers of spin configurations as in Fig. 7b with their time-reversal symmetric. This naturally forms a 32-site magnetic unit cell [Fig. 1a]. We have again 126 temperatures equally spaced between 0 and $0.0025J$. The results are shown in Fig. 8, computed for the same physical parameters mentioned in Sec. III.

These new MC simulations converge nicely and confirm the stability of the ground state found by the machine. The transition is now violently first order, whose hysteresis explains the shift of the transition temperature T_c between $0.8\,10^{-3}J$ in Fig. 3 and $1.5\,10^{-3}J$ in Fig. 8. Quenched simulations in the latter case provide an upper bound of T_c, while slow annealing has more difficulty in finding the ordered phase and provides a lower bound to T_c. The c_1 and c_2 order parameters correctly describe the ground state, with a noticeably stronger finite-size dependence for the latter; a common consequence of the order-by-disorder mechanism.[31] Finally, the order parameter $m_{q=W}$ now saturates at $T = 0$, which means there is a priori no co-existence of other phases.

VI. EMERGENT Z_2 PLANAR SYMMETRY

We now put the machine-learned quantities together and discuss an emergent planar-flip symmetry, which will also resolve the origin of the irregular weights in Fig. 4. For simplicity, we continue to consider the ground state as Fig. 1a as an example, where the order is developed in the xy plane and the planar symmetry acts on spatial xy planes. In general these two planes do not need to coincide, but this does not affect our discussion: the spin-order plane is manifest from the c_1 and c_2 parameters, while the direction of the spatial planar-flip symmetry can be known from the largest weight in d_B.

Given the collinearity on the B-tetrahedron, the decision function Eq. (8) reduces to

$$d_B \sim (-w_1 - w_2 + w_3)^2 = (w_3)^2. \tag{12}$$

Here we have used the solutions in Eqs. (10) and (11) (or equivalently the corresponding configuration in Table I) and the weight relation in Eq. (9). As in this example $\max w_i = w_3 = 1$, the relation Eq. (9) reduces to $w_1 + w_2 = 0$.

Eq. (12) manifests a property of d_B that it is invariant under flipping a specific pair of spins, which can be $(\mathbf{S}_0, \mathbf{S}_3)$ or $(\mathbf{S}_1, \mathbf{S}_2)$ in the current example. Nevertheless, as spins in a B-tetrahedron belong to different A-tetrahedra, in order to preserve the value of the order parameters c_1 and c_2, one has to flip all spins in the two neighbouring A-tetrahedra. This procedure is then repeated to further A-tetrahedra neighbours, and closes only after flipping all A-tetrahedra in an entire layer, as illustrated in Fig. 9.

Namely, there is an *emergent* subsystem symmetry acting on individual ordering layers of A-tetrahedra (equivalently,

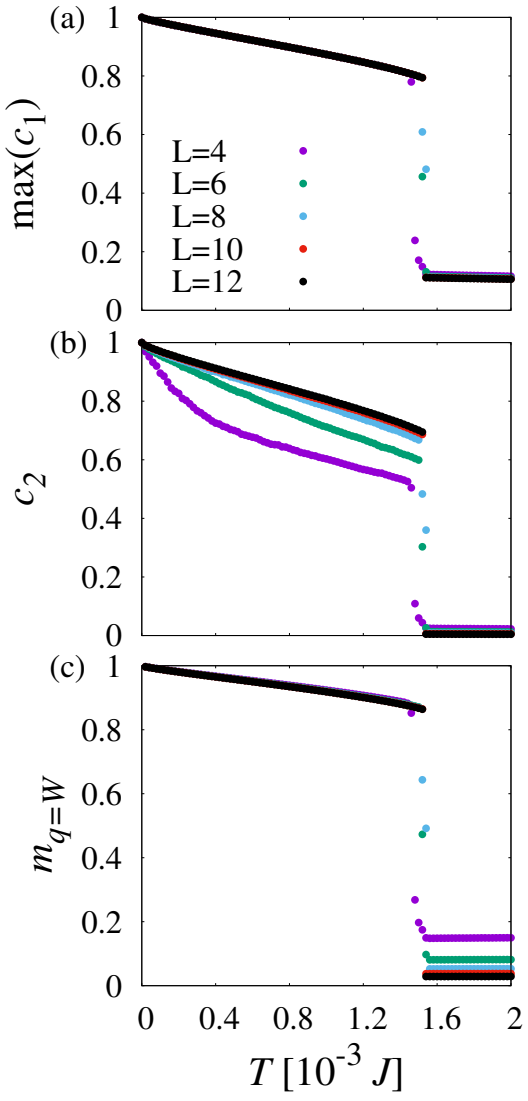

FIG. 8. **Monte Carlo simulations after machine input** shows a phase transition at $T_c \approx 1.5\,10^{-3} J$ in all three order parameters: (a) the average of the maximum value of c_1, (b) c_2 and (c) the order parameter for wavevector $\mathbf{q} = W$ order (corners of the Brillouin zone) for system size $L \in \{4, 6, 8, 10, 12\}$. Simulations have been quenched into the state of Fig. 1a for each temperature.

two adjacent B-tetrahedron layers, while only the bottom or top half of each B-layer is transformed). As a consequence, the system "hybridizes" rank-1 and rank-2 orders. This is a rather unconventional emergent property for an ordered phase; such sub-extensive zero modes usually require to be artificially enforced via either a global or local symmetry of the system[10–12] !

Since this planar spin flip is sub-extensive – it scales as L^2 – we expect it to be dynamically robust. Pragmatically, let's assume that while cooling down the system, such a planar spin flip takes place. This is quite possible since it costs zero energy and the transition is violently first order [Fig. 8]; once the cubic

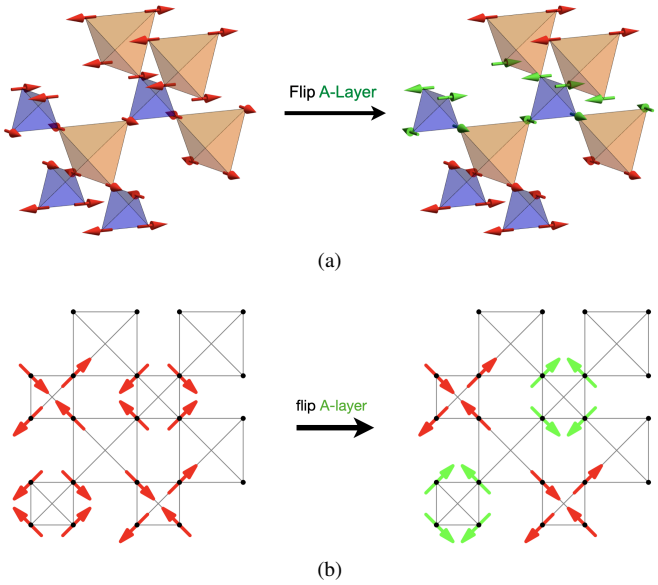

FIG. 9. **Planar Z_2 symmetry.** (a) All A-tetrahedra within one layer are flipped (indicated in green), thereby changing the value of $\mathbf{\Lambda}_E$ in the two neighbouring B-layers. On B-tetrahedra, only intra-layer bonds connecting two A-tetrahedra from the same layer are affected by the transformation. (b) Projection onto the xy-plane; for simplicity not all spins are drawn. This example shows a case where the normal on the spin plane coincides with the normal on the layer-partitioning, but in general we can also construct ground states where the two normals do not coincide.

symmetry is broken in favour of a given plane (here the xy plane), two far-away layers of $A-$tetrahedra may likely order independently from each other. As a result, the long-range dipolar order with Bragg peaks at $\mathbf{q} = W$ found in Fig. 8 will be perturbed by multiple planar spin flips at random positions in the system. And since there is a vanishingly small probability to move L^2 spins coherently in the thermodynamic limit, such energetically degenerate spin configuration should remain stable over very long time scales. This mechanism explains the origin of the irregular weights in Fig. 4, and probably played an important role in the difficulty to interpret previous Monte Carlo simulations, by hindering the ordering mechanism and hiding the magnetic dipolar order. As a result, the magnetic order will be long-range in the plane, but only partial – and possibly even vanishing – in the orthogonal direction. Such states break lattice-rotation symmetry and we dub them "hybridized nematic order", whose director of the nematic state is orthogonal to the planar spin flips.

To conclude, we should mention that among all of the energetically degenerate states connected by Z_2 symmetry, three of them have the 16-site cubic unit cell of Fig. 7b paving the entire lattice. They possess two planar symmetries rather than only one, *e.g.* planar xy- and yz-symmetries with the corresponding weights $w_1 = w_3 = 1, w_2 = -1$, *cf.* table I. But any planar spin flip as in Fig. 9 would immediately break the fragile cubic symmetry.

VII. RELATION TO T_d IRREPS

TKSVM learns order parameters in the language of the raw data, namely, the ordinary spin degrees of freedom. To gain more insight, we can cast the machine-learned quantities in terms of the irreducible representations of the point group T_d,[31] which is the human way of thinking.

At this moment we take a step back and recall the construction of the rank-2 $U(1)$ gauge theory of Refs. 7, 9, 20, and 32 and in particular the fluctuations of the electric field $\mathbf{E}$. Rank-2 $U(1)$ spin liquids satisfy a Gauss law with vectorial character, $\nabla_i E_{ij} = \rho_j$, where $\mathbf{E}$ is a symmetric, traceless rank-2 tensor. Hamiltonians defined as sums of terms living on individual tetrahedra (such as the one considered here) can always be decomposed into (coarse-grained) fields $\mathbf{m}_X$ transforming as the irreps of T_d, the symmetry group of a tetrahedron,[31]

$$H = \frac{1}{2}\sum_{A,X} a_{A,X}\mathbf{m}_X^2 + \frac{1}{2}\sum_{B,X} a_{B,X}\mathbf{m}_X^2, \tag{13}$$

where the $A(B)$ sum runs over all $A(B)$ tetrahedra, and X runs over the irreps $\{A_2, E, T_2, T_{1+}, T_{1-}\}$.[31] In case of the standard Heisenberg antiferromagnet without DM interactions, one has

$$0 < a_{A_2} = a_E = a_{T_2} = a_{T_{1-}} < a_{T_{1+}}. \tag{14}$$

It follows that the fields $\mathbf{m}_{A_2}, \mathbf{m}_E, \mathbf{m}_{T_2}, \mathbf{m}_{T_{1-}}$ are free to fluctuate in the ground state, which can be combined into the rank-2 tensor $\mathbf{E}$. Imposing that $\mathbf{E}$ must be traceless symmetric, and requiring the continuity of the $\mathbf{m}_X$ fields[20] it is necessary to gap out the $\mathbf{m}_{T_2}$ and $\mathbf{m}_{A_2}$ fields on the $A-$tetrahedra, which can be achieved by introducing negative DM interactions on top of the original Heisenberg interactions on the $A-$tetrahedra. Then at low temperature, on $A-$tetrahedra, only the $\mathbf{m}_E$ and $\mathbf{m}_{T1-}$ fields enter into the ground state; $\mathbf{m}_{T_2}$ and $\mathbf{m}_{A_2}$ can be set equal to 0. The resulting tensor electric field is[20]

$$\mathbf{E} = \begin{bmatrix} \frac{2}{\sqrt{3}}m^1_{\mathsf{E}} & m^z_{\mathsf{T}_{1-}} & m^y_{\mathsf{T}_{1-}} \\ m^z_{\mathsf{T}_{1-}} & -\frac{1}{\sqrt{3}}m^1_{\mathsf{E}} - m^2_{\mathsf{E}} & m^x_{\mathsf{T}_{1-}} \\ m^y_{\mathsf{T}_{1-}} & m^x_{\mathsf{T}_{1-}} & -\frac{1}{\sqrt{3}}m^1_{\mathsf{E}} + m^2_{\mathsf{E}} \end{bmatrix}. \tag{15}$$

Furthermore, the condition $\mathbf{m}_{T1+} = 0$ on B-tetrahedra imposes

$$\partial_i E_{ij} = 0 \tag{16}$$

for $\mathbf{E}$ living on the $A-$tetrahedra, which becomes the Gauss law of a rank-2 U(1) theory. This is the Hamiltonian considered in this work.

Going back to the ordered phase of interest in this paper, and using the irreps of a tetrahedron[31] which are reproduced in Table II, the two order parameters found in the decision function in d_A^s can be expressed as

$$c_1^s = \frac{1}{4}(\|\boldsymbol{m}_{T_{1-}}\|^2 + \|\boldsymbol{m}_E\|^2) \tag{17}$$

$$c_2^s = \frac{1}{4}(\|\boldsymbol{m}_{T_{1-}}\|^2 - \|\boldsymbol{m}_E\|^2). \tag{18}$$

We see that c_1^s reproduces the ground-state constraint of the rank-2 $U(1)$ gauge theory, but with an additional index $s \in \{xy, xz, yz\}$ for the spontaneous selection of a spin plane. The order parameter c_2^s is nevertheless an emergent quantity that is not evident from direct symmetry arguments. The meaning of the ground-state condition $c_2^s = \pm 1$ now becomes more intuitive in this irrep basis. Order by disorder ensures that an A-tetrahedron is either fully on $\boldsymbol{m}_{T_{1-}}$ or on $\boldsymbol{m}_E$. The alteration of $c_2^s = \pm 1$ further means that the system can be viewed as staggered layers of $\boldsymbol{m}_{T_{1-}}$ and $\boldsymbol{m}_E$ A-tetrahedra.

For the B-tetrahedron, it is more convenient to use the bond irreps reproduced in Eq. (A1),[33] by which the decision function d_B becomes

$$d_B \sim \left[a_{A_1}\Lambda_{A_1} + a_{E,1}\Lambda_{E,1} + a_{E,2}\Lambda_{E,2}\right]^2, \tag{19}$$

with

$$a_{A_1} = \sqrt{\frac{2}{3}}\,(w_1 + w_2 + w_3) \tag{20}$$

$$a_{E,1} = \sqrt{\frac{1}{3}}\,(2w_1 - w_2 - w_3) \tag{21}$$

$$a_{E,2} = w_2 - w_3. \tag{22}$$

Maximizing d_B then requires $\Lambda_{A_1} \equiv -\sqrt{\frac{2}{3}}$ and that $\boldsymbol{\Lambda}_E$ can only take the following three configurations,

$$\boldsymbol{\Lambda}_E^{\star 1} = \begin{pmatrix} \frac{4}{\sqrt{3}} \\ 0 \end{pmatrix} \quad \boldsymbol{\Lambda}_E^{\star 2} = \begin{pmatrix} \frac{-2}{\sqrt{3}} \\ 2 \end{pmatrix} \quad \boldsymbol{\Lambda}_E^{\star 3} = \begin{pmatrix} \frac{-2}{\sqrt{3}} \\ -2 \end{pmatrix}, \tag{23}$$

which are the three maxima of $\|\boldsymbol{\Lambda}_E\|^2$ under the condition of minimal Λ_{A_1}.

These three configurations are transformed by the Z_2 planar symmetry, as depicted in Fig. 10. Nevertheless, we can infer the distribution of $\boldsymbol{\Lambda}_E$, $\{P(\boldsymbol{\Lambda}_E^{\star 1}), P(\boldsymbol{\Lambda}_E^{\star 2}), P(\boldsymbol{\Lambda}_E^{\star 3})\}$, over all the B-tetrahedra from the weights of d_B in Eq. (8). Specifically, we denote $\boldsymbol{a}_E^{\star 1}, \boldsymbol{a}_E^{\star 2}, \boldsymbol{a}_E^{\star 3}$ to be the respective coefficients in the extreme cases where all B-tetrahedra are in the same $\boldsymbol{\Lambda}_E$ configuration,

$$\boldsymbol{a}_E^{\star 1} = \begin{pmatrix} \frac{-4}{\sqrt{3}} \\ 0 \end{pmatrix}, \quad \boldsymbol{a}_E^{\star 2} = \begin{pmatrix} \frac{2}{\sqrt{3}} \\ -2 \end{pmatrix} \text{ or } \boldsymbol{a}_E^{\star 3} = \begin{pmatrix} \frac{2}{\sqrt{3}} \\ 2 \end{pmatrix}. \tag{24}$$

In addition, $a_{A_1} = \sqrt{2/3}$ reflects the ground state condition $\Lambda_{A_1} = -\sqrt{2/3}$ which is independent of $\boldsymbol{\Lambda}_E$. The general coefficients $a_{A_1}, a_{E,1}, a_{E,2}$ are then solved from a set of linear equations

$$\begin{pmatrix} a_{A_1} & a_{A_1} & a_{A_1} \\ a_{E,1}^{\star 1} & a_{E,1}^{\star 2} & a_{E,1}^{\star 3} \\ a_{E,2}^{\star 1} & a_{E,2}^{\star 2} & a_{E,2}^{\star 3} \end{pmatrix} \begin{pmatrix} P(\boldsymbol{\Lambda}_E^{\star 1}) \\ P(\boldsymbol{\Lambda}_E^{\star 2}) \\ P(\boldsymbol{\Lambda}_E^{\star 3}) \end{pmatrix} = \begin{pmatrix} a_{A_1} \\ a_{E,1} \\ a_{E,2} \end{pmatrix}. \tag{25}$$

Here the first equation reduces to the normalisation of the distribution $\sum_i P(\boldsymbol{\Lambda}_E^{\star i}) = 1$, equivalent to $\sum_i w_i = 1$. In the example of Fig. 7a, the weights are given by $w_1 = -w_2 = 0.4$

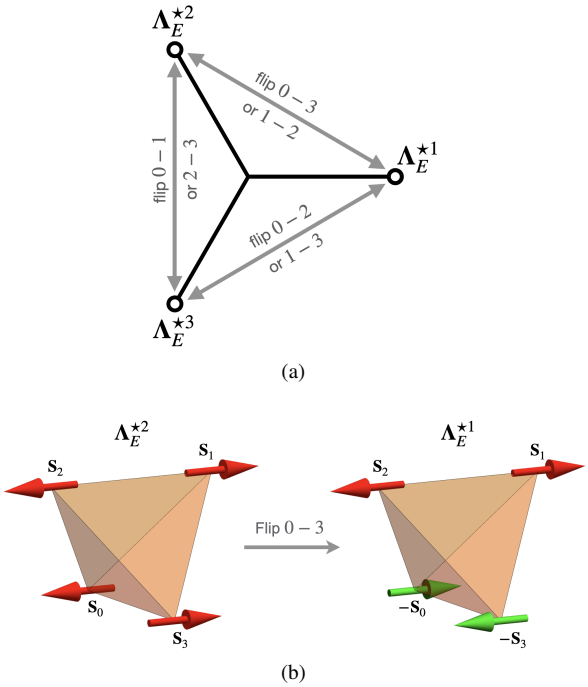

FIG. 10. (a) Triangle formed by the maxima of $\|\mathbf{\Lambda}_E\|^2$ together with the Z_2 bond flip relations. (b) Z_2 symmetry operation acting onto one bond, thereby mapping one maximum to another. Bonds with anti-parallel spins are highlighted in green.

and $w_3 = 1$ which translates to $a_{A_1} = \sqrt{2/3}$, $a_{E,1} = \sqrt{1/3} \cdot 0.2$ and $a_{E,2} = -1.4$. Solving the linear system for these values yields

$$P(\mathbf{\Lambda}_E^{\star 1}) = 0.3 \quad P(\mathbf{\Lambda}_E^{\star 2}) = 0.7 \quad P(\mathbf{\Lambda}_E^{\star 3}) = 0. \tag{26}$$

In general there is always one vanishing $P(\mathbf{\Lambda}_E^{\star i})$, which is equivalent to have maximal weight $\max w_i = 1$ and can be associated with the spatial orientation of the planar Z_2 symmetry, as listed in Table I.

VIII. CONCLUSION

Although artificial intelligence brings the opportunity to automate many of the routine, repeated, tasks which arise in scientific research, it remains an active field of research on how far AI will have an impact on the creative, conceptual, and problem-solving aspects of science. Here, we have shown how poorly thermalised Monte Carlo simulations benefit from cooperation with AI, and how this helped us understand an unconventional and complex magnetic texture. The noisy Monte Carlo data in the unknown phase served as input to the machine, which, at rank 2, discerned certain patterns from which the structure of the phase could be laid bare.

It could be inferred that there are three global spin planes, xy, xz, and yz which spontaneously break the spin rotation symmetry on the A-tetrahedra. The first effective order parameter, c_1, is compatible with the ground state manifold and energy of a single $A-$tetrahedron. Since c_1 can be expressed in terms of the irreps fields $\mathbf{m}_X$ used in the definition of the tensor electric field $\mathbf{E}$ [Eqs. (15) and (17)], it means that the machine was able to extract the relevant degrees of freedom involved in the fluctuations of the rank-2 electric field. This is rather remarkable since the TKSVM algorithm was not taught how the electric field looks like. Instead, it detected the $\mathbf{E}$ fluctuations as a relevant pattern out of noisy numerical data.

The second effective order parameter, c_2, indicates the selection of four specific states [Eq. (6)] out of the U(1) manifold brought to light in the previous step by c_1. This selection cannot be explained by considering $A-$tetrahedra alone since the U(1) manifold is degenerate. It is thus necessarily a consequence of the entropic gain taking place when connecting $A-$tetrahedra together via the intervening antiferromagnetic $B-$tetrahedra. In other words, the ordering mechanism of our model is a thermal order-by-disorder mechanism due to the Gauss-law constraints imposed on the rank-2 electric field.

There is in addition a remaining planar Z_2 subsystem symmetry where flipping all spins on a A-layer leaves its c_2 value invariant. The ground state is thus a rare instance of what we call a "hybridized nematic order", with the co-existence of dipolar (rank-1) and quadrupolar (rank-2) orders due to an emergent subdimensional symmetry.

Our study illustrates how numerical simulations can be enhanced from cooperation with machine learning algorithms. In our case, it was crucial to have a very strongly interpretable algorithm, but also analytical and group-theoretical arguments were indispensable. We do not expect all noisy simulations to be tractable this way. For instance, the critical slowing down witnessed in second-order phase transitions would be especially challenging, since it requires updates acting at different length scales. That being said, our approach is sufficiently general that it can be applied to a variety of complex unknown phases. What immediately comes to mind are other frustrated magnets such as the Kitaev magnets. As the TKSVM algorithm has also been extended to quantum problems,[34] our strategy is not confined to classical physics, and could even be combined with the field of quantum simulation.

The "collaborative" nature of the interactions between human researchers and machines described in this paper become possible wherever the output of machine–learning can be translated into a form which can be understood and manipulated by humans, such as the equations implied by the decision function of a support vector machine. While the TKSVM is ideally suited to such an approach, it is not the only interpretable form of machine learning, and even approaches that are not directly interpretable, such as deep neural networks, may provide critical insights into unsolved problems. As such this model of collaboration offers one possible paradigm for AI-driven research in an age in which human and machine have complementary strengths.

ACKNOWLEDGMENTS

N.S., K.L., and L.P. acknowledge support from FP7/ERC Consolidator Grant QSIMCORR, No. 771891, and the Deutsche Forschungsgemeinschaft (DFG, German Research Foundation) under Germany's Excellence Strategy – EXC-2111 - 390814868. L.D.C.J. acknowledges financial support from CNRS (PICS France-Japan MEFLS) and from the French "Agence Nationale de la Recherche" under Grant No. ANR-18-CE30-0011-01. K.L. acknowledges support from the New Cornerstone Science Foundation through the XPLORER PRIZE, Anhui Initiative in Quantum Information Technologies, and Shanghai Municipal Science and Technology Major Project (Grant No. 2019SHZDZX01). N.S. acknowledges financial support from the Theory of Quantum Matter Unit, OIST, and JSPS KAKENHI Grants No. JP19H05822 and JP19H05825.

Appendix A: Definitions and Conventions

In this Appendix we provide lattice and model definitions, and our conventions for the order parameters of the irreps of the T_d group.

The sites of an A-tetrahedron are located at

$$\boldsymbol{r}_0 = \frac{a}{8}(1,1,1) \qquad \boldsymbol{r}_1 = \frac{a}{8}(1,-1,-1)$$
$$\boldsymbol{r}_2 = \frac{a}{8}(-1,1,-1) \quad \boldsymbol{r}_3 = \frac{a}{8}(-1,-1,1)$$

relative to the center of an A-tetrahedron, as in.[35] Here, a is the length of the FCC unit cell. The sites of a B-tetrahedron are located at $-\boldsymbol{r}_0, -\boldsymbol{r}_1, -\boldsymbol{r}_2, -\boldsymbol{r}_3$ relative to the center of a B-tetrahedron.

The bond dependent DM-interaction vectors are defined as[28,36]

$$\boldsymbol{d}_{01} = \frac{(0,-1,1)}{\sqrt{2}} \quad \boldsymbol{d}_{02} = \frac{(1,0,-1)}{\sqrt{2}} \quad \boldsymbol{d}_{03} = \frac{(-1,1,0)}{\sqrt{2}}$$
$$\boldsymbol{d}_{12} = \frac{(-1,-1,0)}{\sqrt{2}} \quad \boldsymbol{d}_{13} = \frac{(1,0,1)}{\sqrt{2}} \quad \boldsymbol{d}_{23} = \frac{(0,-1,-1)}{\sqrt{2}}$$

In Table II we provide explicit expressions for the order parameters breaking the point-group symmetry of a single tetrahedron,[20,31] used to describe learned TKSVM order parameters on an A-tetrahedron.

In Eq. (A1) below we provide the definition of bond order parameters transforming according to the A_1, E and T_2 irreps.[33] Here the four vectors $\boldsymbol{S}_{0-3}$ refer to the four spins forming a B-tetrahedron.

$$\begin{pmatrix} \Lambda_{A_1} \\ \Lambda_{E,1} \\ \Lambda_{E,2} \\ \Lambda_{T_2,1} \\ \Lambda_{T_2,2} \\ \Lambda_{T_2,3} \end{pmatrix} = \begin{pmatrix} \frac{1}{\sqrt{6}} & \frac{1}{\sqrt{6}} & \frac{1}{\sqrt{6}} & \frac{1}{\sqrt{6}} & \frac{1}{\sqrt{6}} & \frac{1}{\sqrt{6}} \\ \frac{1}{\sqrt{3}} & -\frac{1}{2\sqrt{3}} & -\frac{1}{2\sqrt{3}} & -\frac{1}{2\sqrt{3}} & -\frac{1}{2\sqrt{3}} & \frac{1}{\sqrt{3}} \\ 0 & \frac{1}{2} & -\frac{1}{2} & -\frac{1}{2} & \frac{1}{2} & 0 \\ 0 & 0 & -\frac{1}{\sqrt{2}} & \frac{1}{\sqrt{2}} & 0 & 0 \\ 0 & -\frac{1}{\sqrt{2}} & 0 & 0 & \frac{1}{\sqrt{2}} & 0 \\ -\frac{1}{\sqrt{2}} & 0 & 0 & 0 & 0 & \frac{1}{\sqrt{2}} \end{pmatrix} \begin{pmatrix} \boldsymbol{S}_0 \cdot \boldsymbol{S}_1 \\ \boldsymbol{S}_0 \cdot \boldsymbol{S}_2 \\ \boldsymbol{S}_0 \cdot \boldsymbol{S}_3 \\ \boldsymbol{S}_1 \cdot \boldsymbol{S}_2 \\ \boldsymbol{S}_1 \cdot \boldsymbol{S}_3 \\ \boldsymbol{S}_2 \cdot \boldsymbol{S}_3 \end{pmatrix} \tag{A1}$$

Appendix B: TKSVM

This section aims at providing the reader with the essential working principles of the tensorial-kernel support vector machine (TKSVM). The TKSVM approach is an interpretable and (quasi-)unsupervised machine learning algorithm developed in Refs. 14,16,15 and recently also extended to quantum problems.[34]

Considering classical $O(3)$-spin configurations (ie, Monte Carlo snapshots) $\mathbf{x} = \{S_i^a | i = 1, 2, ..., N; a = x, y, z\}$, the first step of TKSVM is the construction of feature vectors $\boldsymbol{\phi} = \{\phi_\mu\}$ consisting of degree-n monomials from $\mathbf{x}$

$$\phi_\mu = \langle S_{\alpha_1}^{a_1} S_{\alpha_2}^{a_2} \dots S_{\alpha_n}^{a_n} \rangle_{\mathrm{cl}}, \tag{B1}$$

where $\langle \cdots \rangle_{\mathrm{cl}}$ represents a lattice average over pre-determined non-overlapping clusters, each containing r spins, where $\alpha_1, \dots, \alpha_n$ label spins within the cluster, and where $\mu = \{\alpha_1, a_1; \dots; \alpha_n, a_n\}$ denotes a composite index. The tensorial feature space spanned by $\{\phi_\mu\}$ hosts any potential classical spin-order of degree n that fits within the pre-defined cluster of size r. Following the construction of feature vectors from the input data, TKSVM detects the underlying order during the learning stage, provided that the user made a suitable choice of the hyper-parameters n and r. The optimal choice of n and r are unknown a priori. Therefore we choose clusters in accordance with the unit-cell of the lattice and Hamiltonian interactions, and increase n systematically on a trial-and-error basis until TKSVM succeeds. In this approach $n = 1$ allows the detection of magnetic orders, and higher $n > 1$ detects multipolar orders and emergent local constraints.

A central concept of SVM methods is the decision function d. The decision function can be written as a product $d = \mathbf{V}^t \hat{\mathbf{C}} \mathbf{V}$ up to a constant known as the bias. Here, $\mathbf{V}$ is a vector made of input data and $\hat{\mathbf{C}} = \{C_{\mu\nu}\}$ is the output of the machine in the form of a coefficient matrix measuring correlations of ϕ_μ,

$$C_{\mu\nu} = \sum_k \lambda_k \phi_\mu(\mathbf{x}^{(k)}) \phi_\nu(\mathbf{x}^{(k)}), \tag{B2}$$

where the Lagrange multiplier λ_k denotes the weight of the k-th sample. The non-vanishing entries of $C_{\mu\nu}$ identify the relevant basis tensors of the tensorial feature space, and their interpretation yields analytical expressions of the underlying order parameters. As TKSVM has never learned nor seen any of the different phases, it has the advantage of being unbiased in identifying them. Compared to a human approach where one

order parameter	definition in terms of spin components
m_{A_2}	$\frac{1}{2\sqrt{3}}(S_0^x+S_0^y+S_0^z+S_1^x-S_1^y-S_1^z-S_2^x+S_2^y-S_2^z-S_3^x-S_3^y+S_3^z)$
$\mathbf{m}_E$	$\begin{pmatrix}\frac{1}{2\sqrt{6}}(-2S_0^x+S_0^y+S_0^z-2S_1^x-S_1^y-S_1^z+2S_2^x+S_2^y-S_2^z+2S_3^x-S_3^y+S_3^z)\\ \frac{1}{2\sqrt{2}}(-S_0^y+S_0^z+S_1^y-S_1^z-S_2^y-S_2^z+S_3^y+S_3^z)\end{pmatrix}$
$\mathbf{m}_{T_{1+}}$	$\begin{pmatrix}\frac{1}{2}(S_0^x+S_1^x+S_2^x+S_3^x)\\ \frac{1}{2}(S_0^y+S_1^y+S_2^y+S_3^y)\\ \frac{1}{2}(S_0^z+S_1^z+S_2^z+S_3^z)\end{pmatrix}$
$\mathbf{m}_{T_{1-}}$	$\begin{pmatrix}\frac{-1}{2\sqrt{2}}(S_0^y+S_0^z-S_1^y-S_1^z-S_2^y+S_2^z+S_3^y-S_3^z)\\ \frac{-1}{2\sqrt{2}}(S_0^x+S_0^z-S_1^x+S_1^z-S_2^x-S_2^z+S_3^x-S_3^z)\\ \frac{-1}{2\sqrt{2}}(S_0^x+S_0^y-S_1^x+S_1^y+S_2^x-S_2^y-S_3^x-S_3^y)\end{pmatrix}$
$\mathbf{m}_{T_2}$	$\begin{pmatrix}\frac{1}{2\sqrt{2}}(-S_0^y+S_0^z+S_1^y-S_1^z+S_2^y+S_2^z-S_3^y-S_3^z)\\ \frac{1}{2\sqrt{2}}(S_0^x-S_0^z-S_1^x-S_1^z-S_2^x+S_2^z+S_3^x+S_3^z)\\ \frac{1}{2\sqrt{2}}(-S_0^x+S_0^y+S_1^x+S_1^y-S_2^x-S_2^y+S_3^x-S_3^y)\end{pmatrix}$

TABLE II. Order parameters for breaking the point-group symmetry of a single tetrahedron,[20,31] used to describe learned TKSVM order parameters on an A-tetrahedron. The fields $\mathbf{m}_X$ transform according to irreducible representations $A_2, E, T_{1+}, T_{1-}, T_2$ of the tetrahedral point group T_D. The four spins $\mathbf{S}_{0-3}$ forming an A-tetrahedron are located at positions $\mathbf{r}_{0-3}$ defined earlier.

would define an order parameter and then test it on the Monte Carlo data, the approach in TKSVM is blind to specifying order parameter candidates and looks for all possibilities within the search space spanned by the rank-r monomials defined on the cluster of size n.

Appendix C: Pattern Interpretation

The last step of TKSVM consists of constructing the analytical expression of the underlying order from the internal parameters of the learning model. This is achieved by reading off and interpreting the graphical representation (pattern) of the coefficient matrix. Since the underlying order in this case is fairly complex, we shall discuss the procedure for a subset of the full pattern for the A-tetrahedra only. Specifically, we start by considering the block with spin indices $(2\,3, 3\,0)$; see the upper zoomed-in panel of Fig. 5.

Reading off the terms from the block pattern with coefficients approximated as ± 1 yields the expression

$$\begin{aligned}&[d_A]_{(2\,3,3\,0)} \sim \\ &+(S_2^yS_3^x)(S_3^xS_0^x)+(S_2^yS_3^x)(S_3^yS_0^y)-(S_2^xS_3^y)(S_3^xS_0^x)\\ &-(S_2^xS_3^y)(S_3^yS_0^y)+(S_2^yS_3^y)(S_3^xS_0^y)+(S_2^yS_3^y)(S_3^yS_0^x)\\ &-(S_2^xS_3^x)(S_3^xS_0^y)-(S_2^xS_3^x)(S_3^yS_0^x).\end{aligned} \tag{C1}$$

In order to reshape the expression into a sum over square magnitudes of rank-2 order parameters, we factorize the feature components and assign the coefficients (signs) in consistency with other block patterns $(2\,3, 2\,3)$, $(3\,0, 3\,0)$ and $(3\,0, 2\,3)$

$$\begin{aligned}&[d_A]_{(2\,3,3\,0)}+[d_A]_{(3\,0,2\,3)}+[d_A]_{(2\,3,2\,3)}+[d_A]_{(3\,0,3\,0)} \sim \\ &(-S_2^yS_3^x+S_2^xS_3^y-S_3^xS_0^x-S_3^yS_0^y)^2\\ &+(+S_2^xS_3^x-S_2^yS_3^y-S_3^xS_0^y-S_3^yS_0^x)^2.\end{aligned} \tag{C2}$$

We factorize even further, which requires to consider some more block patterns

$$\begin{aligned}&\sum_{ij,i'j'\in\{0,2,3\}}[d_A]_{(i\,j,i'\,j')} \sim \\ &-\left((S_0^x-S_2^y-S_3^x)^2+(S_0^y+S_2^x-S_3^y)^2\right)^2\\ &-\left(2(S_0^x-S_2^y-S_3^x)\cdot(S_0^y+S_2^x-S_3^y)\right)^2.\end{aligned} \tag{C3}$$

This expression already contains a substantial part of the full decision function. Comparing to the definition of c_1^{xy} and c_2^{xy} in eqs. 3 and 4, respectively, reveals that only the terms including $\mathbf{S}_1$ are missing.
Extending the interpretation to the full pattern, we arrive at the expression

$$d_A=\sum_{\substack{ij,i'j'\\ \in\{0,1,2,3\}}}[d_A]_{(i\,j,i'\,j')}\sim-\left((c_1^{xy})^2+(c_2^{xy})^2\right). \tag{C4}$$

Note that the overall minus sign is of technical origin and is arbitrary in each TKSVM run, hence it can be dropped. The sign convention in eq. 2 is chosen to match with the signs in the existing definition of $\mathbf{m}_{T_{1-}}$, see its third component in Table II for comparison. Furthermore a factor of $1/16$ was introduced to normalize the order parameters to 1 when saturated (deep in phase).

[1] C. Castelnovo, R. Moessner, and S. L. Sondhi, Nature **451**, 42 (2008).
[2] L. Jaubert and M. Udagawa, eds., *Spin Ice*, Springer Series in Solid-State Sciences, Vol. 197 (Springer, 2021).
[3] M. Hermele, M. P. A. Fisher, and L. Balents, Phys. Rev. B **69**, 064404 (2004).
[4] S. D. Pace, S. C. Morampudi, R. Moessner, and C. R. Laumann, Physical Review Letters **127**, 117205 (2021).
[5] A. Kitaev, Annals of Physics **321**, 2 (2006).
[6] M. Hermanns, I. Kimchi, and J. Knolle, Annual Review of Condensed Matter Physics **9**, 17 (2018).
[7] M. Pretko, Physical Review B **96**, 035119 (2017).
[8] A. Prem, S. Vijay, Y.-Z. Chou, M. Pretko, and R. M. Nandkishore, Physical Review B **98**, 165140 (2018).
[9] A. Rasmussen, Y.-Z. You, and C. Xu, Stable gapless bose liquid phases without any symmetry (2016), arXiv:1601.08235 [cond-mat.str-el].
[10] R. M. Nandkishore and M. Hermele, Annual Review of Condensed Matter Physics **10**, 295 (2019).
[11] M. Pretko, X. Chen, and Y. You, International Journal of Modern Physics A **35**, 2030003 (2020).
[12] A. Gromov and L. Radzihovsky, Rev. Mod. Phys. **96**, 011001 (2024).
[13] J. Carrasquilla and R. G. Melko, Nature Physics **13**, 431 (2017).
[14] K. Liu, J. Greitemann, and L. Pollet, Physical Review B **99**, 104410 (2019), number: 10.
[15] J. Greitemann, K. Liu, L. D. C. Jaubert, H. Yan, N. Shannon, and L. Pollet, Phys. Rev. B **100**, 174408 (2019).
[16] J. Greitemann, K. Liu, and L. Pollet, Physical Review B **99**, 060404 (2019), number: 6.
[17] B. Olsthoorn, J. Hellsvik, and A. V. Balatsky, Phys. Rev. Res. **2**, 043308 (2020).
[18] D. Lozano-Gómez, D. Pereira, and M. J. P. Gingras, Phys. Rev. Res. **4**, 043118 (2022).
[19] K. Liu, N. Sadoune, N. Rao, J. Greitemann, and L. Pollet, Phys. Rev. Res. **3**, 023016 (2021).
[20] H. Yan, O. Benton, L. D. C. Jaubert, and N. Shannon, Phys. Rev. Lett. **124**, 127203 (2020).
[21] E. Z. Zhang, F. L. Buessen, and Y. B. Kim, Phys. Rev. B **105**, L060408 (2022).
[22] E. Shender, Sov. Phys. JETP **56**, 178 (1982).
[23] C. L. Henley, Phys. Rev. Lett. **62**, 2056 (1989).
[24] T. Haku, K. Kimura, Y. Matsumoto, M. Soda, M. Sera, D. Yu, R. A. Mole, T. Takeuchi, S. Nakatsuji, Y. Kono, T. Sakakibara, L.-J. Chang, and T. Masuda, Phys. Rev. B **93**, 220407 (2016).
[25] J. G. Rau, L. S. Wu, A. F. May, L. Poudel, B. Winn, V. O. Garlea, A. Huq, P. Whitfield, A. E. Taylor, M. D. Lumsden, M. J. P. Gingras, and A. D. Christianson, Phys. Rev. Lett. **116**, 257204 (2016).
[26] L. E. Chern, Y. B. Kim, and C. Castelnovo, Phys. Rev. B **106**, 134402 (2022).
[27] M. Taillefumier, O. Benton, H. Yan, L. D. C. Jaubert, and N. Shannon, Phys. Rev. X **7**, 041057 (2017).
[28] B. Canals, M. Elhajal, and C. Lacroix, Phys. Rev. B **78**, 214431 (2008).
[29] G.-W. Chern, arXiv (2010), arXiv:1008.3038 [cond-mat.str-el].
[30] V. Noculak, D. Lozano-Gomez, J. Oitmaa, R. R. P. Singh, Y. Iqbal, M. J. P. Gingras, and J. Reuther, Physical Review B **107**, 214414 (2023).
[31] H. Yan, O. Benton, L. Jaubert, and N. Shannon, Phys. Rev. B **95**, 094422 (2017).
[32] M. Pretko, Phys. Rev. B **95**, 115139 (2017).
[33] N. Shannon, K. Penc, and Y. Motome, Phys. Rev. B **81**, 184409 (2010).
[34] N. Sadoune, G. Giudici, K. Liu, and L. Pollet, Phys. Rev. Res. **5**, 013082 (2023).
[35] K. A. Ross, L. Savary, B. D. Gaulin, and L. Balents, Physical Review X **1**, 021002 (2011).
[36] V. N. Kotov, M. Elhajal, M. E. Zhitomirsky, and F. Mila, Phys. Rev. B **72**, 014421 (2005).